



UNIVERSITY OF LEEDS

This is a repository copy of *Stochastic analysis of dynamic stress amplification factors for slab track foundations*.

White Rose Research Online URL for this paper:

<https://eprints.whiterose.ac.uk/196926/>

Version: Accepted Version

Article:

Xie, H, Luo, Q, Wang, T et al. (2 more authors) (2023) Stochastic analysis of dynamic stress amplification factors for slab track foundations. *International Journal of Rail Transportation*. ISSN 2324-8378

<https://doi.org/10.1080/23248378.2023.2170286>

© 2023 Informa UK Limited, trading as Taylor & Francis Group. This is an author produced version of an article published in *International Journal of Rail Transportation*. Uploaded in accordance with the publisher's self-archiving policy.

Reuse

Items deposited in White Rose Research Online are protected by copyright, with all rights reserved unless indicated otherwise. They may be downloaded and/or printed for private study, or other acts as permitted by national copyright laws. The publisher or other rights holders may allow further reproduction and re-use of the full text version. This is indicated by the licence information on the White Rose Research Online record for the item.

Takedown

If you consider content in White Rose Research Online to be in breach of UK law, please notify us by emailing eprints@whiterose.ac.uk including the URL of the record and the reason for the withdrawal request.



eprints@whiterose.ac.uk
<https://eprints.whiterose.ac.uk/>

Stochastic analysis of dynamic stress amplification factors for slab track foundations

Hongwei Xie ^a, Qiang Luo ^{a,b}, Tengfei Wang ^{a,b,*}, Liangwei Jiang ^{a,b}, David P. Connolly ^c

^a *School of Civil Engineering, Southwest Jiaotong Univ., Chengdu 610031, China*

^b *MOE Key Laboratory of High-Speed Railway Engineering, Chengdu 610031, China*

^c *School of Civil Engineering, University of Leeds, Leeds LS2 9JT, UK*

*Corresponding author: w@swjtu.edu.cn

Abstract

The relationship between railway track-bed stresses and speed is essential when performing railway track and foundation design. Current approaches to describe this relationship are typically empirical and multiply the static track response by a dynamic amplification factor to account for (dynamic) speed effects. This paper develops an alternative method for dynamic amplification factor generation instead of numerical simulation. A vehicle–track dynamics model is presented, capable of simulating the dynamic effects induced in subgrade in the presence of random track irregularities. To perform a stochastic analysis, first samples of irregularity are generated based upon a mean vertical track profile power spectral density. A range of train speeds and track-spectrum cumulative probabilities are computed using the numerical model before analyzing the resultant surface stresses. The resulting dynamic amplification factors follow a Gumbel distribution, with their means and standard deviations increasing nonlinearly with increased speed and track-spectrum cumulative probability. Data normalization is performed before showing the development of a bespoke dynamic amplification function for the site under analysis. Based on speed, track-spectrum cumulative probability, and p -values, the proposed model yields dynamic amplification predictions within 5% of the simulated values.

Keywords: Railway slab track; track-bed stress; vehicle–track coupled dynamics; track irregularity; stochastic analysis, Dynamic amplification factor

1. Introduction

It is important to consider vehicle–track interaction when designing track structures, particularly for trains traveling at high speeds. Concrete slab tracks are widely used on high-speed rail (HSR) lines because of their advantages over ballasted tracks in terms of reduced maintenance requirements and the possibility of more extended possession periods [1,2]. HSR lines must be longitudinally uniform and consistent, and the track-bed must be dynamically stable. Track substructures (roadbeds) are constructed with geotechnical materials that have varying properties. Their stability can be influenced by loading [3] and environmental factors [4,5], so these are critical to consider when performing track foundation design. Current design methods for railway earth structures commonly approximate dynamic loads by multiplying the static load by a dynamic amplification factor (DAF) greater than 1.0 [6]. Therefore, an important aspect of track foundation design is applying accurate DAFs. The DAF is also used for the design of other geostructures, such as retaining wall [7] and piled embankment [8,9].

In addition to DAFs, dynamic wheel load factors have received considerable attention among industry and academia for a long time [10]. Dynamic wheel loads have been predicted using a variety of methods, and a substantial number of these methods were empirically developed based on field data from their respective modes of rail transportation [11]. These predictive methods consider several factors, such as track loading, health, and rolling stock design. Historically, most research has focused on evaluating dynamic impact loads for heavy-axle-loading freight trains, in part due to the widespread deployment of wheel impact load detectors on heavy-axle-loading freight railroad corridors in North America. For DAFs of track foundations, most predictive methods are empirically developed as a function of train speed that accounts for factors such as curves, track conditions, and track type [12,13]. Track irregularities are not sufficiently considered and assessed from a probabilistic perspective in these DAF methods, which require further investigation.

Field instrumentation can directly measure the dynamic response of track foundations during train passage. According to measurements during the commissioning and testing of the Beijing–Shanghai HSR [14], the concrete base displacement increased from 0.05 mm to 0.11 mm as the train speed increased from 100 km/h to 400 km/h. Field testing [15–17] on the Suining–Chongqing railway (slab track) showed the upper limit of the 95% confidence interval for the surface stresses of foundations

increased by approximately 100% when travel speed increased from 5 km/h to 200 km/h. As observed in field geotechnical instrumentation, the measured dynamic stress on the foundation surface of the Wuhan–Guangzhou HSR increased from 2.03 kPa to 3.21 kPa when the speed increased from 200 km/h to 350 km/h [18], increasing by 58%. For the Beijing–Shenyang HSR operating at 250–350 km/h, the measured stress ranges from 17.4 kPa to 18.8 kPa, with DAFs of 1.2–1.25 [19]. Although in-situ testing is useful, it is only a spot measurement, can be challenging to perform to high precision and can only be used after track construction.

Alternatively, large scale laboratory tests can also be used to study the behavior of railway infrastructure systems under moving loads. For example, Bian et al. [20] developed a full-scale ballastless railway model to investigate track structure response and soil foundations under train moving loads. It was found that the DAFs at foundation surface level increased nonlinearly with train speed. The DAF for the surface stress of the track foundation was 1.08 when speeds increased from 300 to 360 km/h. Instead of physical modeling, numerical modelling can also be used [21]. For example, an equivalent dynamic model based on the finite element method [19] yielded DAFs of 1.25–1.35 for speeds ranging from 200 to 350 km/h. The simulation results also showed that as train speed increased from 200 to 350 km/h, the displacement amplitude on the roadbed surface increased from 0.33 mm to 0.40 mm, and the stress increased from 14.2 kPa to 15.1 kPa [22]. Alternatively, a track-ground model [23,24] was used to study DAFs for differing subgrade conditions. It was further extended to include non-linear soil stiffness and damping behavior [25].

The majority of these aforementioned studies have ignored dynamic effects generated due to wheel/rail interaction, assuming the largest contribution to DAFs is due to increases in quasi-static excitation with speed. However, depending upon the track geometry quality, which governs train-track interaction, this may not always be true. To allow for the analysis of track geometry most rail administrations measure it using inspection cars equipped with automatic recording systems. The data is statistically analyzed for peaks and standard deviations, which are compared against technical specifications [26–28].

The numerical simulation of vehicle–track coupled dynamics [29–36] commonly considers the system as stochastic with randomness characterized by excitation sources and system configurations.

Railway system performance in service lifecycle phases changes as operating time increases and degrades due to the time-variant parameters. However, advances in the study of stochastic vehicle–track dynamics are rarely applied to assess track foundations.

The goal of this study is to estimate the train-induced surface stresses of slab track foundations from the perspective of stochastic modeling. To this end, we present a numerical method based on vehicle–track coupled dynamics that incorporates random track irregularities into the prediction of DAFs. The stochastic characteristics of dynamic stress on roadbed surfaces are then assessed against the train speed and PSD probability level. Finally, a normalized predictive model for DAF is tested with different train speeds and PSD probability levels.

2. Vehicle-track coupled dynamics model

Figure 1 shows the numerical model used to simulate a moving train on railway slab track, which established by Zhai [29,31]. The track and vehicle are modeled as linear systems with nonlinearity interaction between rails and wheels. The simulation approach uses separate track and vehicle sub-models, coupled using the wheel/rail contact forces. Complete details of the model are given in [29].

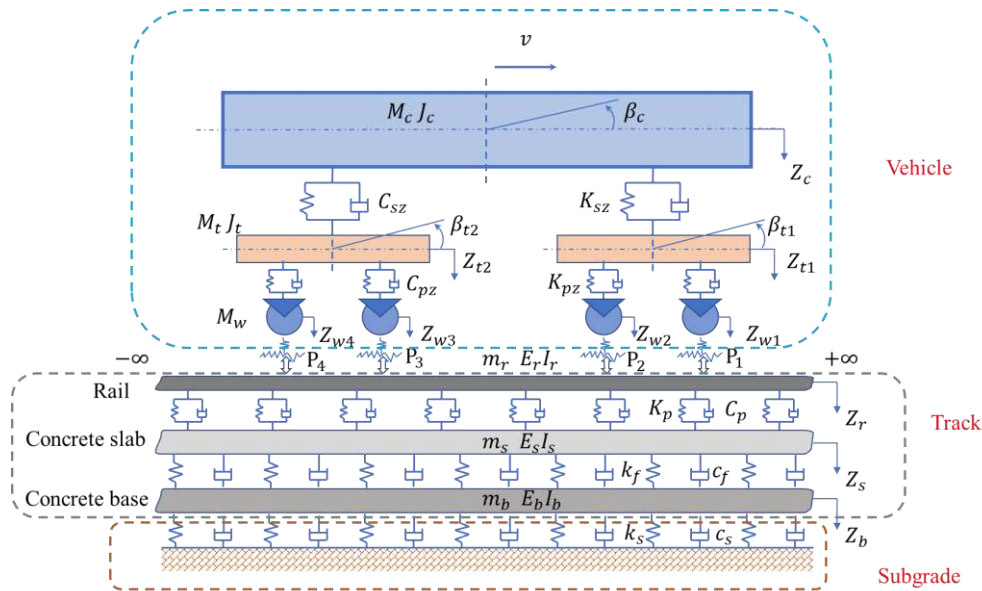


Figure 1. Vehicle–track coupled vertical dynamics model

2.1. Computational model and parameters

The vehicle model is based on a mass-spring-damper multi-rigid-body system with four axles, four wheelsets, two bogie frames, and two layers of suspension. The rigid bodies (car body, wheelsets,

and bogie frames) have two degrees of freedom, including pitch and bounce motions as a function of their centre of mass. The vehicle system therefore has 10 degrees of freedom. The vehicle in the simulation is reproduced from the electric multiple unit rail cars manufactured by the CRRC Qingdao Sifang (M2) as part of the CRH380A train. An additional live load of 85 passengers is considered (i.e., 8 t), with other dynamic parameters provided in Table 1.

Table 1. Dynamic vehicle parameters

Parameters	Notation/(unit)	Value
Car body mass + loading	M_c /(kg)	34,934+8,000
Mass moment of the inertia of the car body	J_c /(kg·m ²)	1.711 8×10 ⁶
Bogie mass	M_t /(kg)	3,300
Mass moment of the inertia of the bogie	J_t /(kg·m ²)	1,807
Wheelset mass	M_w /(kg)	1,780
Stiffness coefficient of the primary suspension	K_{pz} /(N·m ⁻¹)	1.176×10 ⁵
Damping coefficient of the primary suspension	C_{pz} /(N·s·m ⁻¹)	1.0×10 ⁴
Stiffness coefficient of the secondary suspension	K_{sz} /(N·m ⁻¹)	2.4×10 ⁵
Damping coefficient of the secondary suspension	C_{sz} /(N·s·m ⁻¹)	2.0×10 ⁴
Semi-longitudinal distance between bogies (m)	L_c /(m)	8.75
Semi-longitudinal distance between wheelsets in a bogie	L_t /(m)	1.25
Static axle load	P_0 /(kN)	138.9
Wheel radius	R /(m)	0.43

The slab track comprises rails, track slabs, and concrete bases, all modeled as Euler–Bernoulli beams. The rail beam is supported by a series of discrete fastener points on the track slabs, and the spacing of neighboring points equals the span of two fasteners. The track slabs and concrete base are bonded by a functional layer formed by self-compacting concrete (SCC). The concrete base is placed on the foundation (also called the roadbed or formation). It is assumed the fastener pad functions as a spring-damper element, while the SCC layer and subgrade act as layers of continuously distributed spring-dampers. The dimensions and material properties of the track–subgrade system are summarized

in Table 2. The track structure length is 306.18 m (54 track slabs), and the simulation operating distance is 220 m.

Table 2. Properties of the slab track system

Principal component	Parameter	Notation/(unit)	Value
Rail	Elastic modulus	$E_r/(\text{N}\cdot\text{m}^{-2})$	2.059×10^{11}
	Area moment of the rail cross-section	$I_r/(\text{m}^4)$	3.217×10^{-5}
	Mass per unit length	$m_r/(\text{kg}\cdot\text{m}^{-1})$	60.64
Fastener	Stiffness	$K_p/(\text{N}\cdot\text{m}^{-1})$	3.75×10^7
	Damping	$C_p/(\text{N}\cdot\text{s}\cdot\text{m}^{-1})$	3.625×10^4
	Spacing	$l_s/(\text{m})$	0.63
Track slab	Length	$L_s/(\text{m})$	5.6
	Width	$B_s/(\text{m})$	2.5
	Height	$H_s/(\text{m})$	0.3
	Density	$\rho_s/(\text{kg}\cdot\text{m}^{-3})$	2600
SCC layer	Stiffness per unit length	$k_f/(\text{N}\cdot\text{m}^{-2})$	1.25×10^9
	Damping per unit length	$c_f/(\text{N}\cdot\text{s}\cdot\text{m}^{-2})$	8.3×10^4
Concrete base	Length	$L_b/(\text{m})$	16.99
	Width	$B_b/(\text{m})$	3.1
	Height	$H_b/(\text{m})$	0.3
	Density	$\rho_b/(\text{kg}\cdot\text{m}^{-3})$	2500
Subgrade	Stiffness per unit length	$k_s/(\text{N}\cdot\text{m}^{-2})$	1.7×10^8
	Damping per unit length	$c_s/(\text{N}\cdot\text{s}\cdot\text{m}^{-2})$	1.5×10^5

Based on the theory of vehicle–track coupling dynamics [29], the equations of motion for a vehicle–track interaction system are:

$$\begin{bmatrix} \mathbf{M}_V & 0 \\ 0 & \mathbf{M}_T \end{bmatrix} \begin{Bmatrix} \ddot{\mathbf{X}}_V \\ \ddot{\mathbf{X}}_T \end{Bmatrix} + \begin{bmatrix} \mathbf{C}_V & 0 \\ 0 & \mathbf{C}_T \end{bmatrix} \begin{Bmatrix} \dot{\mathbf{X}}_V \\ \dot{\mathbf{X}}_T \end{Bmatrix} + \begin{bmatrix} \mathbf{K}_V & 0 \\ 0 & \mathbf{K}_T \end{bmatrix} \begin{Bmatrix} \mathbf{X}_V \\ \mathbf{X}_T \end{Bmatrix} = \begin{Bmatrix} \mathbf{F}_V \\ \mathbf{F}_T \end{Bmatrix} \quad (1)$$

where the subscripts V and T represent the vehicle and track, respectively; and \mathbf{M} , \mathbf{X} , \mathbf{C} , \mathbf{K} , and \mathbf{F}

denote the submatrices of mass, displacement vectors, damping, stiffness, and load vectors, respectively. Using Hertzian non-adhesive elastic contact theory, the wheel/rail contact force is:

$$P_j(t) = \begin{cases} \left[\frac{1}{G} \delta Z_j(t) \right]^{3/2}, & \delta Z_j(t) > 0 \\ 0, & \delta Z_j(t) \leq 0 \end{cases} \quad (2)$$

where G is the constant of wheel-rail contact and $\delta Z_j(t)$ denotes the elastic deformation of the j^{th} wheel, expressed as:

$$\delta Z_j(t) = Z_{wj}(t) - Z_r(x_{wj}, t) - \eta_{0j}(t) \quad (3)$$

where t denotes the time; $Z_{wj}(t)$ is the vertical displacement of the j^{th} wheel; $Z_r(x_{wj}, t)$ is the vertical displacement of the rail; and $\eta_{0j}(t)$ is the vertical geometric irregularity between the surface of the j^{th} wheel and the rail.

2.2. Simulation of random track irregularities

2.2.1. Probabilistic characteristics of PSD

Power spectral density (PSD) characterizes the frequency content of a signal, and is commonly used to interpret track geometry data. The purpose of spectral-density estimation (SDE) in statistical signal processing is to estimate the spectrum of a random signal based on a sequence of time samples. For a discrete digital signal $x[n]$, of non-zero duration $x(t)$, the discrete-time Fourier transform (DTFT) can be used to estimate PSD's $\hat{S}[k]$, for signals such as measured track irregularities:

$$\hat{S}[k] = \frac{1}{N^2} X[k] X^*[k] = \frac{1}{N} |X[k]|^2 \quad (4)$$

where $X[k]$ is the DTFT of $x[n]$, $X[k] = \sum_{n=0}^{N-1} x[n] e^{-j[2\pi/N]kn}$, and N is the length of $x[n]$.

The variance of this estimate can be computed by observing that the finite Fourier transform $X[k]$ is composed of a series of components at various frequencies $f = k/N, k = 1, 2, 3, \dots$. Note that $X[k]$ is a complex number, with its real and imaginary parts, $X_R[k]$ and $X_I[k]$ respectively, which are uncorrelated random variables with equal variances and zero means. The Fourier transformation is a linear operation, meaning $X_I[k]$ and $X_R[k]$ become Gaussian random variables if $x(t)$ is Gaussian. Thus, the quantity:

$$|X[k]|^2 = X_R^2[k] + X_I^2[k] \quad (5)$$

equals the sum of the squares of two independent Gaussian variables. Consequently, each frequency

component of the estimate $S[k/N]$ will have a sampling distribution per the chi-squared distribution:

$$\frac{\hat{S}[k/N]}{S[f=k/N]} = \frac{\chi_2^2}{2}, k = 1, 2, 3, \dots \quad (6)$$

where χ_2^2 is the chi-square variable with two DOFs. Due to the similarity of the PSD functions for track irregularities, one may set the PSD line as a function of track-spectrum cumulative probability λ and spatial frequency $\omega = f/v$:

$$S(\omega, \lambda) = \frac{F^{-1}(\lambda|\chi_2^2)}{2} \bar{S}(\omega) \quad (7)$$

where $F^{-1}(\lambda|\chi_2^2)$ is the inverse distribution function (quantile function) for χ_2^2 and $\bar{S}(\omega)$ is the mathematical expectation of $S(\omega)$ at spatial frequency ω . Note that the cumulative probability for mean of chi-square variable with two DOFs (χ_2^2) is 0.632, indicating that $\lambda = 0.632$ for $\bar{S}(\omega)$.

2.2.2. PSD of HSR track irregularities

Track irregularities generate wheel/rail forces and induce the propagation of stress waves, which cause structural deterioration, including differential settlement [37]. The four most common types of track irregularities are: vertical profile, alignment, cross-level, and gauge. Vertical profile most significantly influences the dynamic response of the subgrade [6].

Power functions can be used to fit the PSD of China's HSR ballastless track irregularities [38], and then the mean PSD of the track irregularities can be obtained by:

$$\bar{S}(\omega) = \frac{A}{\omega^\alpha} \quad (8)$$

where A and α are the regression coefficients, which correspond to the intercept and slope of the segmented line of the PSD curve in the *log-log* coordinate system, as shown in Figure 2. For the vertical profile, A , α , and segmentation points are provided in Table 3.

Table 3. Mean PSD parameters of the China HSR slab-track vertical profile.

Segment number	A	α	segmented point (1/m)
(1)	1.0544×10^{-5}	3.3891	—
(2)	3.5588×10^{-3}	1.9271	0.0187
(3)	1.9784×10^{-2}	1.3643	0.0474
(4)	3.9488×10^{-4}	3.4516	0.1533

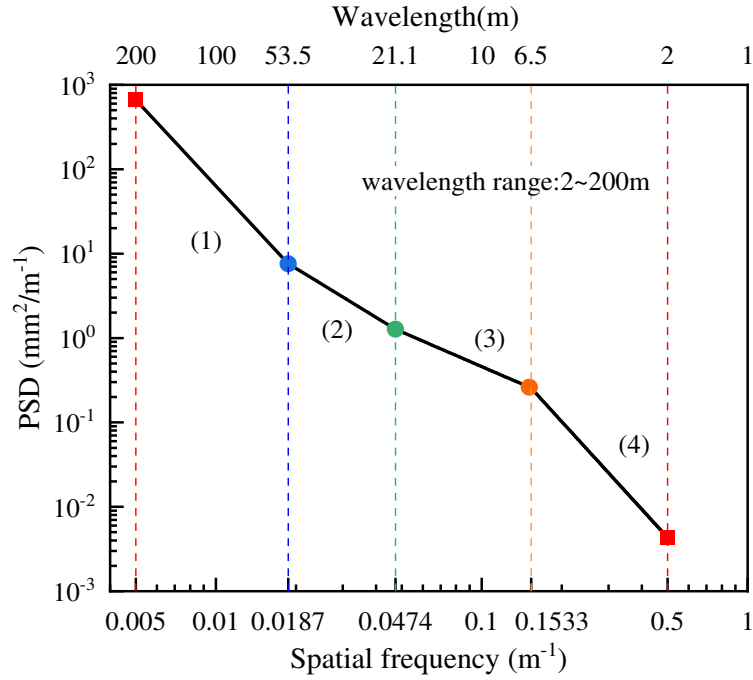


Figure 2. Mean PSD of the track vertical profiles

The inverse Fourier transform method (IFTM) [39] is used to determine the time-domain track random irregularities with the same amplitude-frequency characteristics $S(\omega)$. Figure 3 shows the application of the IFTM to the mean PSD of a slab track vertical profile, whose wavelength range is 2–200 m.

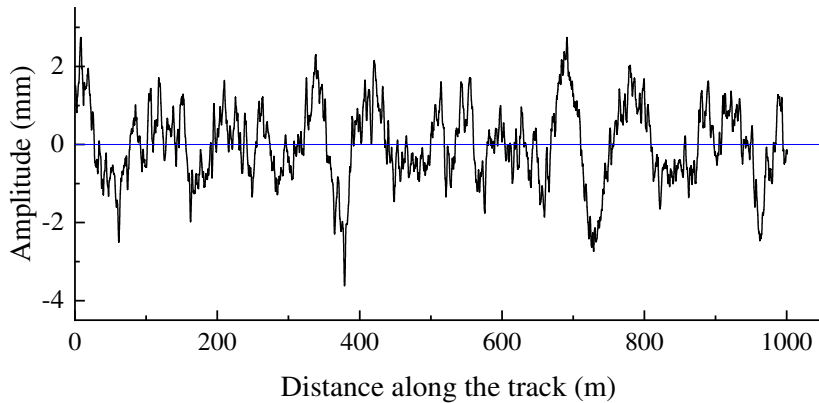


Figure 3. Random vertical irregularity excitation samples generated by IFTM

2.3. Model validation

Field monitoring programs were undertaken on the Beijing–Shanghai HSR (Line 1), Beijing–Tianjin intercity rail (Line 2), and Wuhan–Guangzhou HSR (Line 3) to measure the dynamic responses (vibration and stress) of their earth structures (track foundation). Two train sets, CRH-2 and

CRH-3 (China Railway High-speed), were used as test trains.

Table 4 provides the data measured during train passage and alternative simulation results calculated using a Green's function approach [22]. The reported simulation model follows the technical specifications of CRH-2 at an operating speed of 300 km/h. And its track irregularities generated by the China ballastless track average spectrum ($\lambda=0.632$). The model results of wheel/rail contact force, rail displacement, and road surface stress are similar to the simulated data at speeds of 300 km/h; the calculated surface displacement, velocity, and acceleration by the proposed approach fall within the observed values in Rail Lines 1 to 3. The consistency between measured, simulated, and modeled values shows the accuracy of dynamics modeling.

Table 4. Comparison between measured and simulated values of ballastless track dynamic response

Scenarios	Line 1 [14]	Line 2 [40]	Line 3 [40]	Simulation [22]	This study
Speed range (km/h)	74–424	45–389	150–360	300	300
Wheel/rail force (kN)	\	\	\	84.6	85.15
Rail displacement (mm)	\	\	\	1.3	1.34
Surface stress of foundation (kPa)	\	\	0.9–19.3	14.6	14.03
Displacement at foundation surface (mm)	0.0–0.3	0.01–0.41	0.9–19.3	0.42	0.36
Velocity at foundation surface (mm/s)	0.2–30.9	0.17–4.64	0.7–11.2	\	10.35
Surface acceleration of foundation (m ² /s)	0.0–6.6	0.01–6.02	0.11–3.70	4.3	3.51

3. Probabilistic characteristics of dynamic stress on foundation surface

To incorporate track irregularities into an alternative method for dynamic amplification factor, the vertically coupled dynamics model (Figure 1) was used to obtain the dynamic stress response of the roadbed induced by a moving train load in the presence of track irregularities at average level ($\lambda = 0.632$). The value of λ is prescribed as 0.632 for $\bar{S}(\omega)$ because the cumulative probability for mean of chi-square variable with two DOFs (i.e., χ_2^2) is 0.632.

3.1. Longitudinal distribution pattern

Figure 4a-c presents example time histories of fastener force, stress in the SCC layer and on the roadbed surface, where positive values denote compression. Similarly, Figure 4d-f presents the

corresponding Fourier transforms at operating speeds of 5 km/h, 250 km/h, and 400 km/h. The origin of the coordinate is set as the position where the first axle of the vehicle was located.

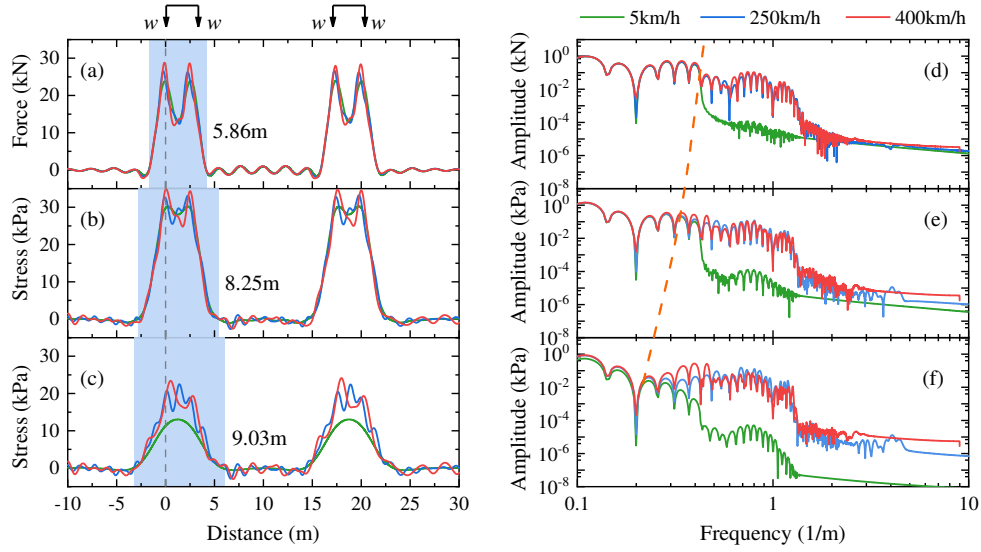


Figure 4. Typical dynamic response of track structure and subgrade: (a) fastener force; (b) SCC stress; (c) subgrade stress; (d) spectrum of fastener force; (e) spectrum of SCC stress; (f) spectrum of subgrade stress.

As shown in Figure 4, the dynamic response longitudinal distribution form gradually transformed from the double-peak "M" shape, dominated by axle loads at the fastener position, to the single-peak "A" dominated by bogie loads on the roadbed surface. The influencing length of a bogie on the roadbed stress increased from approximately 5.86 m to 9.03 m. Because of geometric and material damping, the peak dynamic stress gradually decreased with increasing distance between the structural layers and rails. When the vehicle's speed increased, the dynamic effect increased accordingly. For example, the dynamic response of each structural layer exhibited higher-frequency content, and the peak dynamic stress in the SCC and foundation increased significantly. This effect extended to a lower frequency range as the distance between the structural layer and the wheel/rail interface increased.

The behavior of slab track for HSR can be approximated as a laminated beam. When a uniaxial load W acts on the rails, the reaction force on the foundation surface under the slab track is computed by [41]

$$\sigma(x) = \frac{W\xi}{2b} e^{-\xi|x|} [\cos(\xi|x|) + \sin(\xi|x|)] \quad (9)$$

where b is the width of a concrete base, x is the longitudinal coordinate of the action point, and ξ is a constant calculated by Equation (10), which relates to the foundation stiffness k per meter and slab-

track bending stiffness EI .

$$\xi = \sqrt[4]{\frac{k}{4EI}} \quad (10)$$

Figure 5 depicts the longitudinal distribution of the static stress calculated by Equation (9), measured dynamic stress for 65 km/h (instrumentation with earth pressure cells), and simulated dynamic stress for 150 km/h on the roadbed surface along with double-axle loads. These two speeds are considered for representing quasi-static and dynamic scenarios. The loading and unloading process of train load stress corresponds to the passage of a bogie with two axles [6]. When the train was traveling at a low speed (65 km/h), the static stress obtained from Equation (9) is consistent with the measured subgrade-borne stress. This is due to the almost negligible dynamic amplification. When the vehicle speed increased to 150 km/h, the average dynamic stress increased. The variation of dynamic stresses at the same relative location is primarily caused by different irregularity in different locations, and follows a normal distribution.

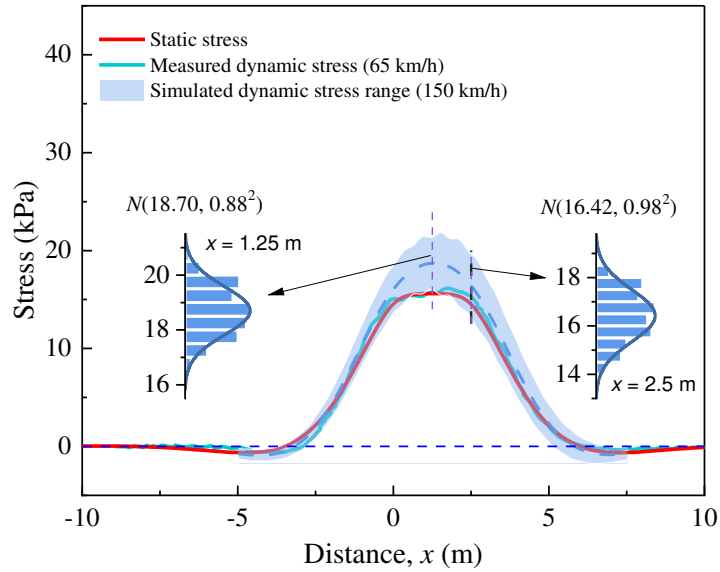


Figure 5. Distribution of subgrade stress along the relative operation distance

3.2. Extreme value probability characteristics

The amplification effect of subgrade-borne vibrations due to running trains is often characterized by a dynamic amplification factor (DAF), defined as the ratio of the dynamic stress amplitude σ_d to the static stress amplitude σ_0 on the roadbed surface. It is given by:

$$\phi = \frac{\sigma_d}{\sigma_0} \approx \frac{\sigma_d}{\sigma_5} \quad (11)$$

where ϕ denotes the DAF, σ_5 denotes dynamic stress amplitude at 5 km/h.

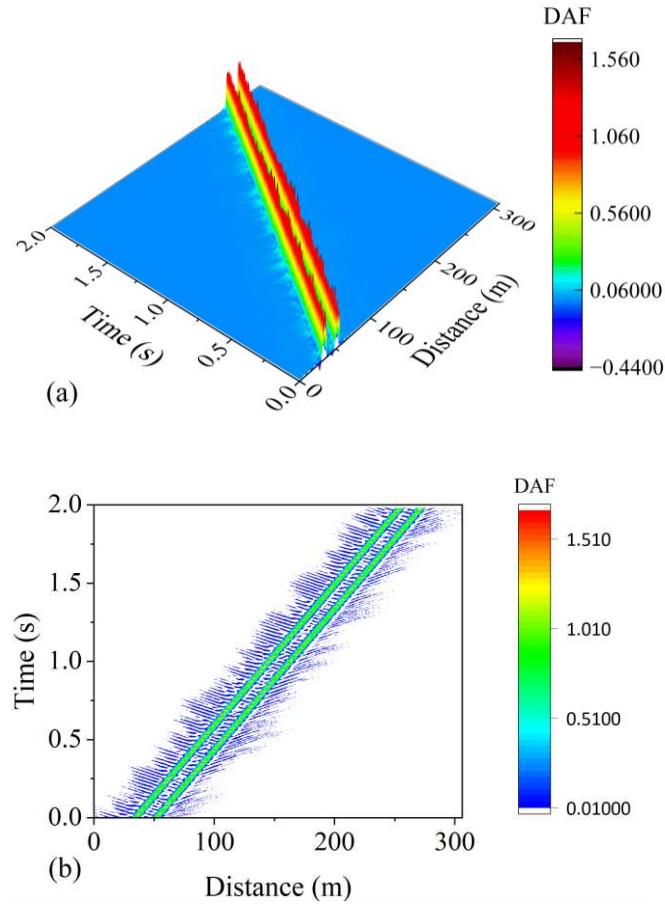


Figure 6. Spatiotemporal distribution of DAF ($\lambda = 0.632$, $v = 400$ km/h): (a) perspective view; (b) plane view

DAFs fluctuate along a certain line due to the presence of random wheel-rail irregularities. To quantify the randomness, dynamic simulations were performed considering a vehicle traveling at 400 km/h on a slab track with track irregularities following an average level ($\lambda = 0.632$). Figure 6 shows the simulated DAFs, calculated by Equation (11). The dataset was established by taking 634 DAF samples over the roadbed surface under 317 fasteners. It should be noted that the fasteners contained two dynamic stress peaks and hence generated two DAF samples. The histogram and empirical cumulative distribution of DAFs are shown in Figure 7. It shows a positively skewed distribution pattern, with a statistical skewness of 0.667, mean of 1.263, and standard deviation of 0.138.

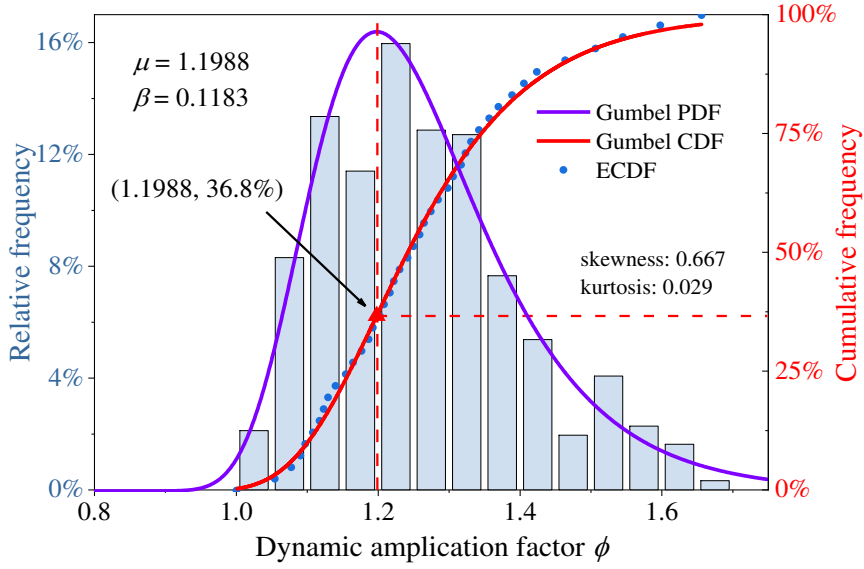


Figure 7. Empirical probability distribution of DAFs

The amplitude of dynamic stresses on roadbed surfaces obeys a normal distribution, as Figure 5 shown. Extreme values generated from a normal random variable follow the Gumbel distribution (also known as the extreme value Type I distribution). This means the maximum values of independent and identically distributed random variables of the initial normal distribution converge to the Gumbel distribution [42]. A time history of subgrade dynamic stress is a sampling of subgrade dynamic responses at different loading positions, and the peaks occur at random locations. The DAF associated with peak stress naturally obeys the Gumbel distribution. Equation (12) shows its cumulative distribution function (CDF) $F(\phi)$, which is a double exponential function.

$$F(\phi; \mu, \beta) = \exp \left[- \exp \left(- \frac{\phi - \mu}{\beta} \right) \right] \quad (12)$$

where μ and β are the location and scale parameters for Gumbel distribution, respectively. μ reflects the overall level of ϕ . β is the scale parameter, which is a measure of the dispersion of ϕ and characterizes the variability of ϕ along the route.

Fitting the empirical cumulative distribution function (ECDF) in Figure 7 with the Gumbel CDF using the nonlinear least square fitting method yields the position parameter $\mu = 1.1988$ and scale parameter $\beta = 0.1183$. The estimated PDF (probability density function) and CDF curves are also shown in Figure 7, and are well matched. Ref. [43] indicates the peak dynamic stresses on the

foundation surface should obey a normal distribution. The Kolmogorov–Smirnov (K–S) test was used to examine the distribution. The K–S test indicator D_N for the normal distribution, shown in Table 5, is greater than the critical value $D_{N,0.95}$, while D_N for the Gumbel distribution is less than the critical value $D_{N,0.95}$. ϕ does not obey the normal distribution; instead, the Gumbel distribution was confirmed at a significance level of 0.05.

Table 5. Kolmogorov–Smirnov test for the DAFs

Distribution type	K-S statistic D_N	$D_{N,0.95}$	Decision at level (0.05)
Normal distribution	0.061	0.054	Reject
Gumbel distribution	0.032	0.054	Can't reject

For four operating permutations: $v = 350$ km/h (maximum speed in commercial operation) and 400 km/h (maximum design speed in operation), and $\lambda = 0.632$ and 0.99, the data are fitted using normal and Gumbel distributions. The goodness of fit is shown in Table 6. Compared with the normal distribution, the Gumbel distribution has a significantly lower residual sum of squares, and better describes the empirical distribution of DAFs.

Table 6. Comparison of the goodness of fit for normal and Gumbel distributions

v (km/h)	λ	Mean	S.D.	μ	β	SSE	R^2	RMSE	Distribution
350	0.632	1.227	0.1261	/	/	0.6230	0.9882	0.0314	Normal
400	0.632	1.249	0.1342	/	/	0.3062	0.9942	0.0220	
350	0.99	1.509	0.2697	/	/	0.6411	0.9878	0.0319	
400	0.99	1.547	0.2851	/	/	0.2581	0.9951	0.0202	
350	0.632	/	/	1.179	0.1076	0.0798	0.9985	0.0112	Gumbel
400	0.632	/	/	1.198	0.1185	0.1040	0.9980	0.0128	
350	0.99	/	/	1.407	0.2306	0.0808	0.9985	0.0113	
400	0.99	/	/	1.438	0.2526	0.1056	0.9980	0.0129	

4. Predictive models of surface stress

4.1. Track-spectrum cumulative probability

To characterize the extent of track irregularity, track-spectrum cumulative probability λ is employed. Static inspection of track irregularity is primarily done using the mid-chord offset (MCO) method [44] or multipoint chord reference (MCR) method [45]. In contrast, dynamic collection of the data using track inspection cars usually employs band-pass filtering. Determine the management value for each sample of irregularities with the help of bisection method, as shown in Table 7. For regular maintenance, temporary repair, and when a speed limit of 200 km/h is imposed, λ approximately equals 0.95, 0.9999, and 0.999996, respectively. λ corresponds to the track unevenness management values ranging from 0.50 to 0.99.

Table 7. Cumulative probabilities of uneven management values

Method	Management level	Value (mm)	λ
MCO method (10 m)	Works acceptance	2	0.556 3
MCO method (10 m)	Regular maintenance	4	0.957 2
MCO method (10 m)	Temporary repair	7	0.999 9
MCO method (10 m)	Speed limit, 200 km/h	8	~ 1.000
MCR method (5 m/30 m)	/	2	0.575 8
MCR method (150 m/300 m)	/	10	0.906 5
Band-pass filtering method (1.5–42 m)	I	3	0.957 1
Band-pass filtering method (1.5–42 m)	II	5	0.999 8
Band-pass filtering method (1.5–120 m)	I	5	0.985 4
Band-pass filtering method (1.5–120 m)	II	7	0.999 7

4.2. Probability distribution and normalized expressions

The track construction type and line speed can influence the dynamic effects of train operation. Japan [12], Germany [13], and China [6] have proposed estimation equations for the equivalent DAF of stresses. In addition to train speed, track smoothness influences the dynamic response of a vehicle–track–subgrade coupled system. As the rail-surface smoothness deteriorates, the forces induced due to train/track dynamic interaction increase and the DAF rises.

In the simulations, the train running speed (v) was taken as 5 (quasi-static), 50, 100, 150, 200, 250, 300, 350, 400, 450, and 500 km/h; λ for the track irregularity spectrum was prescribed as 0.00, 0.10, 0.25, 0.50, 0.60, 0.632, 0.70, 0.75, 0.80, 0.90, 0.95, and 0.99, yielding a total of 132 simulation scenarios. The simulated surface stress of the roadbed under $v = 5$ km/h (quasi-static) were taken as the reference value. Then, Equation (11) was used to calculate the DAFs. The empirical distribution of

DAF under each simulation scenario was fitted using Equation (12), yielding the Gumbel distribution's location parameter μ and scale parameter β , with R^2 values greater than 0.95. That indicated the Gumbel distribution could be used with reasonable accuracy. The distributions of μ and β in the binary variable space comprising train speed v and cumulative probability λ are illustrated in Figs. 8 and 9.

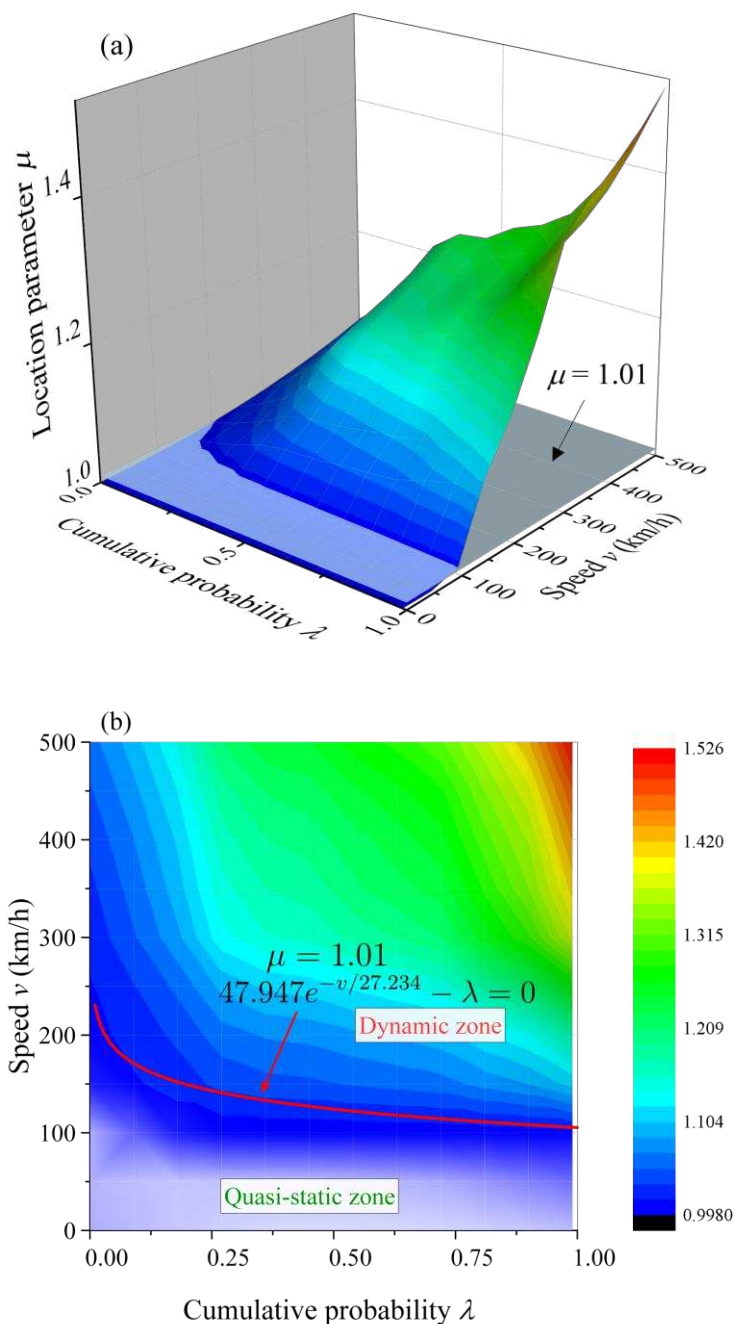


Figure 8. Contours of location parameter μ : (a) general view; (b) top view

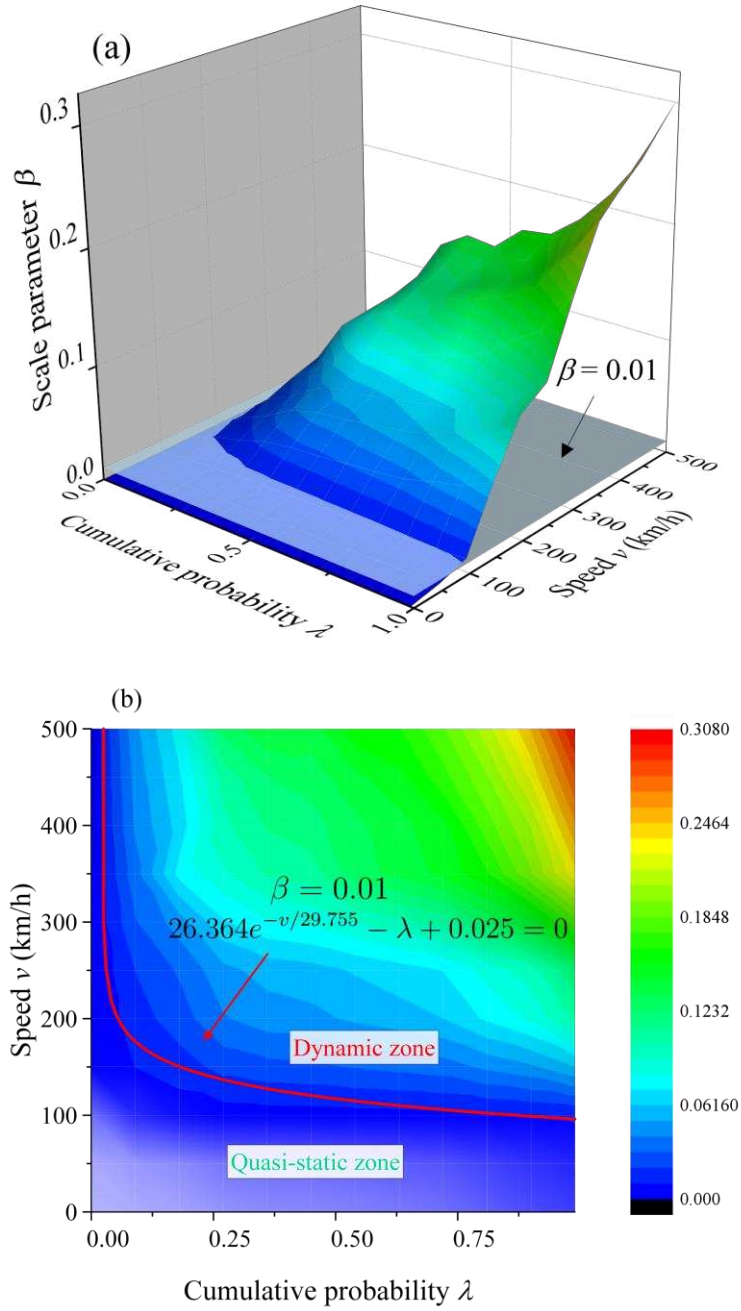


Figure 9. Contours of scale parameter β : (a) general view; (b) top view

The dynamic response was almost insignificant when the train speed was low or the rail was had minimal irregularities. The (v, λ) space could be divided into two portions, quasi-static and dynamic zones, by taking Equation (13) for $\mu = 1.01$ or Equation (14) for $\beta = 0.01$ as the boundaries. As speed increased and track irregularity deteriorated, the position parameter μ and scale parameter β gradually increased. Also, DAF increased, while its dispersion was also more significant.

$$47.95e^{-v/27.23} - \lambda = 0 \quad (13)$$

$$26.36e^{-v/29.76} - \lambda + 0.025 = 0 \quad (14)$$

4.2.1. Influence of vehicle speed

Considering identical track irregularities, a higher speed produces more pronounced variations in wheel/rail interaction and a greater DAF. Figure 10a shows the location parameter μ against the speed v , which shows the curves with different λ values had a similar pattern. The location parameters converge to 1.0 when v is close to 0 km/h. In Figure 10b, the scale parameter β follows the same trend and converges to 0 as v approaches 0 km/h. Be noted that speeds > 500 km/h may induce the critical velocity effect [21,46–48], challenging for the presented spring-dashpot type track model to simulate. Researchers are encouraged to examine the critical velocity effect before employing the proposed method for the dynamic stress amplification factors at very high operating speeds.

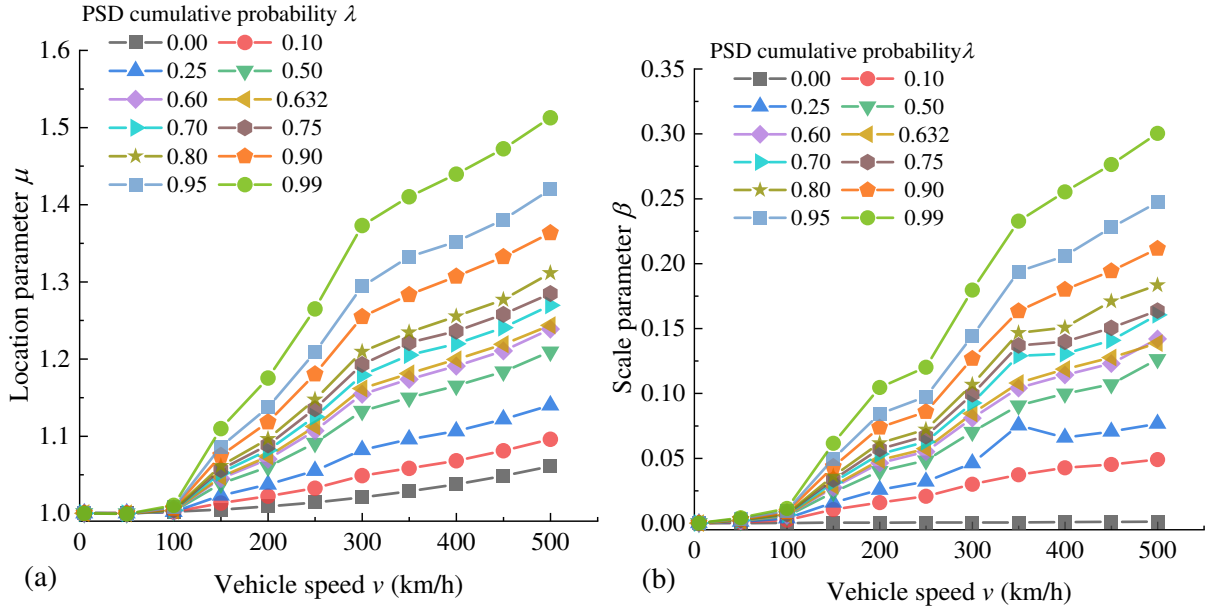


Figure 10. Probability distribution parameter comparisons for vehicle speed: (a) location parameter; (b) scale parameter

The probability properties of the DAFs concerning train speed were normalized using two parameters: the location-speed index $I_{\mu v}$ and the scale-speed index $I_{\beta v}$. The two indices relate to the location parameter and scale parameter, respectively, which are expressed as:

$$I_{\mu v} = \frac{\mu(v, \lambda) - \mu(0, \lambda)}{\mu(400, \lambda) - \mu(0, \lambda)} = \frac{\mu(v, \lambda) - 1}{\mu(400, \lambda) - 1} \quad (15)$$

$$I_{\beta v} = \frac{\beta(v, \lambda) - \beta(0, \lambda)}{\beta(400, \lambda) - \beta(0, \lambda)} = \frac{\beta(v, \lambda)}{\beta(400, \lambda)} \quad (16)$$

where $\mu(0, \lambda)$, $\mu(400, \lambda)$, $\beta(0, \lambda)$, and $\beta(400, \lambda)$ are the location parameters and scale parameters at $v = 0$ and 400 km/h, in which $v = 0$ indicates no dynamic effect. Thus, $DAF = 1.0$ is obtained at $v = 0$ km/h regardless of λ , indicating that $\mu(0, \lambda) = 1$ and $\beta(0, \lambda) = 0$.

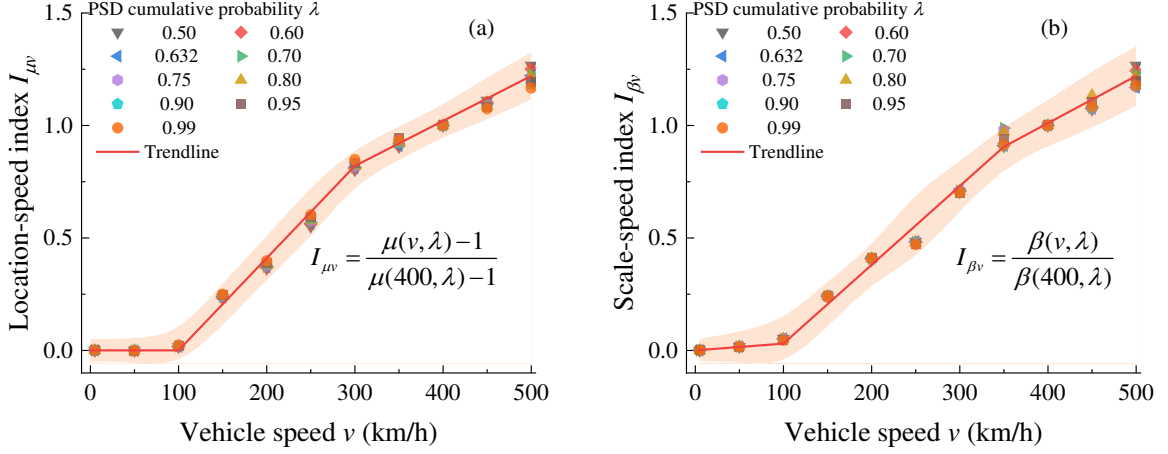


Figure 11. Normalization of probability distribution parameters with respect to vehicle speed: (a) location parameter; (b) scale parameter

Figure 11 plots the location-speed and scale-speed indices against speed. All data points were distributed around a trend line within a narrow band for both location and scale-speed indices. The trend lines are defined by Equations (17) and (18). Note that when v was less than 100 km/h, the dynamic effect was small enough to be ignored, so it can be assumed: $I_{\mu v} \approx 0$.

$$I_{\mu v} = \begin{cases} 0 & v \in (0, 100] \text{ km/h} \\ 0.0041v - 0.41 & v \in (100, 300] \text{ km/h} \\ 0.002v + 0.22 & v \in (300, 500] \text{ km/h} \end{cases} \quad (17)$$

$$I_{\beta v} = \begin{cases} 0.0003v & v \in (0, 100] \text{ km/h} \\ 0.0035v - 0.32 & v \in (100, 350] \text{ km/h} \\ 0.0021v + 0.17 & v \in (350, 500] \text{ km/h} \end{cases} \quad (18)$$

The dynamic effect of trains on the HSR slab track foundation under consideration can be described using threshold speeds. For example, when $v < 100$ km/h, the subgrade-borne dynamic effect is not significant and the static axle load of a train is dominant. However, when v exceeded 100 km/h, the DAFs grow nonlinearly.

At low speeds, the vibration energy at the wheel/rail interface was low and damped as it propagated into the track structure. Approximately the same dynamic stress was experienced on the roadbed surface as static stress at low operating speeds. With increasing speed, the energy input to the

coupling system increased, the vibration of the track structure intensified, the dynamic effect gradually became more significant, and the surface stress of the foundation increased accordingly.

4.2.2. Influence of track irregularity

Track irregularity, acting as system excitation, is another important factor that affects the dynamic response of a vehicle–track coupling system. Figure 12 displays a family of curves and their normalizations for probability parameters of DAF versus λ at different speeds. Regardless of the speed, both the location parameter μ and the scale parameter β show increased nonlinearly with λ .

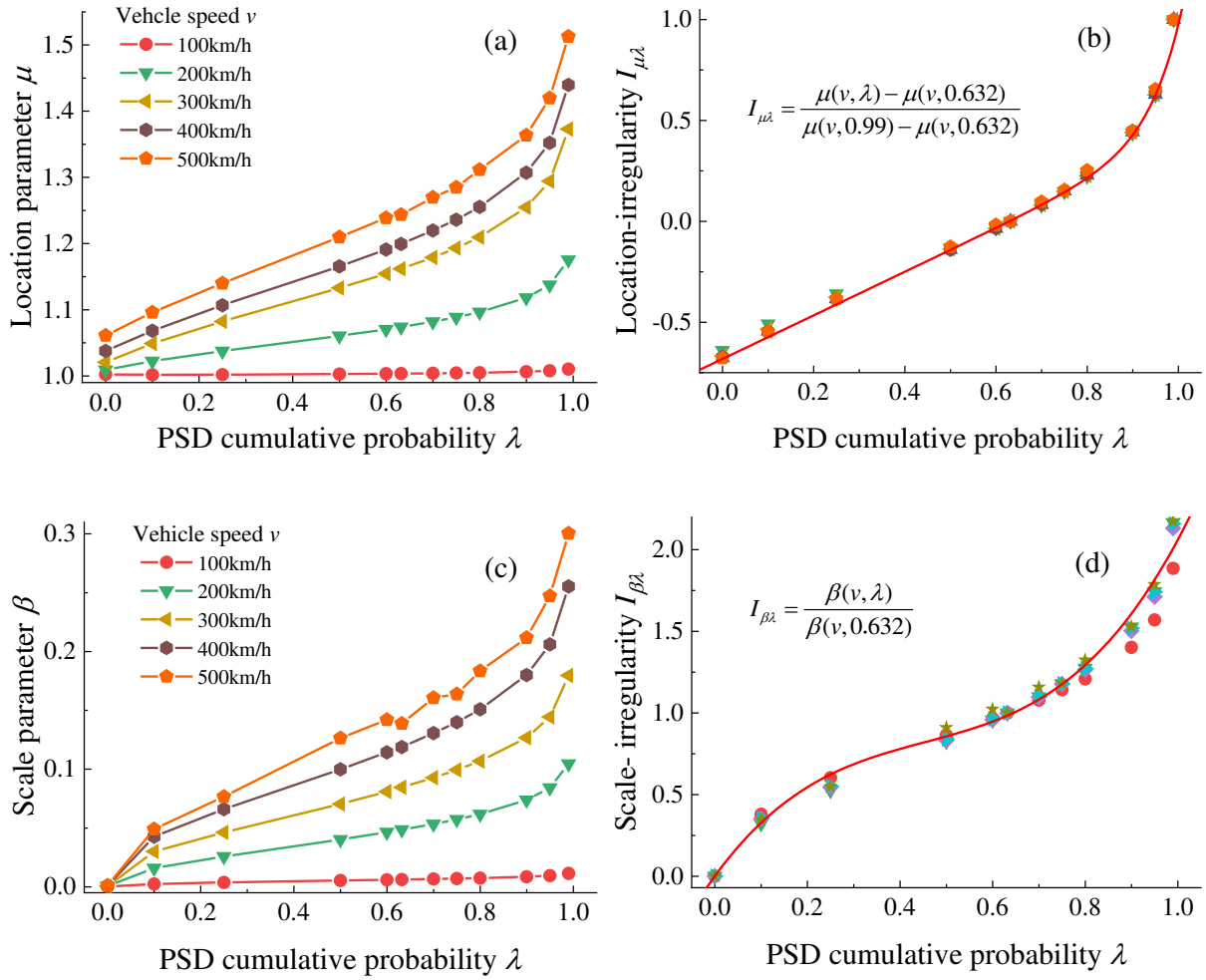


Figure 12. Normalization of probability distribution parameters with respect to PSD cumulative probability: (a) location parameter; (b) central tendency irregularity index; (c) scale parameter; (d) dispersion-irregularity index.

The normalizations were performed by introducing the location-irregularity index $I_{\mu\lambda}$ and scale-irregularity index $I_{\beta\lambda}$, as shown in Equations (19) and (20). For the location-irregularity index $I_{\mu\lambda}$, λ

= 0.632 and $\lambda = 0.99$ were set as the characteristic points. For the scale-irregularity index $I_{\beta\lambda}$, $\lambda = 0$ and $\lambda = 0.632$ were set as the characteristic points. $\beta(v, 0) = 0$ refers to the case without irregularities.

$$I_{\mu\lambda} = \frac{\mu(v,\lambda) - \mu(v,0.632)}{\mu(v,0.99) - \mu(v,0.632)} \quad (19)$$

$$I_{\beta\lambda} = \frac{\beta(v,\lambda) - \beta(v,0)}{\beta(v,0.632) - \beta(v,0)} = \frac{\beta(v,\lambda)}{\beta(v,0.632)} \quad (20)$$

In Figure 12, the location-irregularity index $I_{\mu\lambda}$ increased approximately linearly with λ when λ was low. When $\lambda > 0.632$, $I_{\mu\lambda}$ started to increase more rapidly. A function with linear and exponential components was used to fit $I_{\mu\lambda}$, as expressed by Equation (21), with $R^2 = 0.9916$.

$$I_{\mu\lambda} = 1.08(\lambda - 0.632) + 0.003 \exp\left(\frac{\lambda - 0.632}{0.07}\right) \quad (21)$$

The curve of the scale-irregularity index $I_{\beta\lambda}$ versus λ is an inverse S-shaped pattern and is fitted with a cubic polynomial, expressed using Equation (22) with $R^2 = 0.9856$.

$$I_{\beta\lambda} = 3.91\lambda - 6.94\lambda^2 + 5.09\lambda^3 \quad (22)$$

4.3. Three-parameter predictive model for DAFs

Assuming v and λ have independent effects on subgrade dynamic stress, binary functions of v and λ are established based on the probability distribution parameters μ and β for the DAFs, which are denoted: $\mu(v, \lambda)$ and $\beta(v, \lambda)$.

The normalized Equations (19) and (21) for the location-speed index $I_{\mu v}$ and location-irregularity index $I_{\mu\lambda}$, are combined and solved to determine $\mu(v, \lambda)$. Given the characteristic point information $\mu(400, 0.99) = 1.4397$ and $\mu(400, 0.632) = 1.1994$, the location parameter μ can be obtained as:

$$\begin{aligned} \mu(v, \lambda) &= I_{\mu v} I_{\mu\lambda} [\mu(400, 0.99) - \mu(400, 0.632)] \\ &\quad + I_{\mu v} [\mu(400, 0.632) - 1] + 1 \\ &= 0.2403 I_{\mu v} I_{\mu\lambda} + 0.1994 I_{\mu v} + 1 \end{aligned} \quad (23)$$

Similarly, Equations (20) and (22) of the scale-speed index $I_{\beta v}$ and scale-irregularity index $I_{\beta\lambda}$ are solved together to calculate $\beta(v, \lambda)$. Then, the general expression (24) of the scale parameter β is obtained considering the characteristic points $\beta(400, 0.632) = 0.1187$.

$$\beta(v, \lambda) = I_{\beta v} I_{\beta\lambda} \beta(400, 0.632) = 0.1187 I_{\beta v} I_{\beta\lambda} \quad (24)$$

With speeds of 0–500 km/h and λ of 0–0.99, the estimated values of μ and β are derived from Equations (23) and (24). The differences are less than 6% compared with the simulated values, as

shown in Table 8.

Table 8. Parameter residual of the probability distribution of DAF

Statistical parameter	Minimum residual	Maximum residual
μ	-0.0111 (-0.80%)	0.0349 (2.54%)
β	-0.0254 (-5.42%)	0.0162 (4.42%)

The likelihood that the DAF does not exceed ϕ is designated p . The quantile concerning $F(\phi) = p$ is inverted from Equation (12). A description of DAF as a function of speed v , cumulative probability λ , and p can be expressed as:

$$\phi(v, \lambda, p) = \mu(v, \lambda) + \beta(v, \lambda) \cdot \ln\left(-\frac{1}{\ln(p)}\right) \quad (25)$$

For the average ($\lambda = 0.632$) and critical ($\lambda = 0.99$) level of track irregularity, if the speed is between 200 km/h and 500 km/h, the quantile values $\phi(v, \lambda, p)$ for the DAFs are calculated using Equation (25). As shown in Table 9, three probabilities were involved: 57.0% (Gumbel mean value), 75.0% (Q3), and 95%. Compared with the simulated values, the maximum DAF error was 0.05, and the maximum relative error was 3.4%, demonstrating a high prediction accuracy.

Table 9. Comparison of predicted and simulated values of DAFs

v (km/h)	λ	$p=57.0\%$		$p=75.0\%$		$p=95.0\%$	
		Prediction	Simulation	Prediction	Simulation	Prediction	Simulation
200	0.632	1.11	1.10	1.14	1.13	1.21	1.22
	0.99	1.22	1.24	1.28	1.31	1.44	1.49
300	0.632	1.22	1.21	1.27	1.27	1.43	1.41
	0.99	1.44	1.48	1.56	1.60	1.88	1.91
350	0.632	1.25	1.24	1.32	1.32	1.51	1.50
	0.99	1.51	1.54	1.66	1.70	2.05	2.10
400	0.632	1.27	1.27	1.36	1.35	1.57	1.55
	0.99	1.56	1.59	1.73	1.76	2.16	2.20
500	0.632	1.33	1.32	1.43	1.42	1.68	1.66
	0.99	1.67	1.69	1.87	1.89	2.39	2.41

Ref. [6] presents design values of subgrade DAF as 1.9 and 1.3 for 300 km/h HSR. The counterparts are $\phi(300, 0.99, 95\%) = 1.87$ and $\phi(300, 0.632, 75\%) = 1.27$ respectively, as shown in Table 9. Further, Bian et al. [20] conducted a full-scale model test of a ballastless high speed track under simulated train moving loads, and the measured subgrade DAF at 300 km/h was 1.08. This model did not account for track irregularity, indicating $\lambda = 0$. While $\phi(300, 0, 75\%) = 1.08$ indicates

that Equation (25) for subgrade DAF is consistent. Considering similar irregularity levels and probabilities, the design DAFs for 400 km/h can be obtained, which are $\phi(400, 0.99, 95\%) = 2.16$ and $\phi(400, 0.632, 75\%) = 1.36$ respectively.

4.4. Conditional probability distribution of DAFs

In practical situations, it is difficult to determine the track irregularity spectrum cumulative probability λ , especially in the absence of measured irregularity data. Considering that the track irregularity spectrum follows a χ_2^2 distribution, the DAF probability distribution can be derived from the law of total probability.

Assuming the cumulative probability of the track irregularity spectrum is λ at an operating speed of v , Equation (25) produces $\phi(v, \lambda, p)$, corresponding to the cumulative probability p ($p = P\{\Phi < \phi | \Lambda = \lambda, v\}$, where Φ denotes the random variable for DAFs, and Λ denotes the random variable of λ). The probability distribution of DAFs $F_\Phi(\phi | v)$ can be considered the marginal distribution of the joint distribution $F_{\Lambda, \Phi}(\lambda, \phi | v)$ under the law of total probability. It can be derived from the conditional probability density function $f_{\Lambda | \Phi}(\lambda | \phi, v)$, expressed as:

$$\begin{aligned} F_\Phi(\phi | v) &= P\{\Phi < \phi | v\} = \int_1^\phi \int_0^1 f_{\Lambda, \Phi}(\lambda, \phi | v) d\lambda d\phi \\ &= \int_0^1 \int_1^\phi f_{\Phi | \Lambda}(\phi | \lambda, v) f_\Lambda(\lambda) d\phi d\lambda \\ &= \int_0^1 P\{\Phi < \phi | \Lambda = \lambda, v\} f_\Lambda(\lambda) d\lambda \end{aligned} \quad (26)$$

In reality, adjacent railroad line sections have similar maintenance and geological conditions. They have similar frequency characteristics of track irregularity, meaning that λ varies slightly, and the track irregularity has spatial frequency coherence. To describe the DAF probability distribution for the proximity intervals, the conditional probability DAF distribution function for λ in the range $[a, b]$ is defined using:

$$F_\Phi(\phi | [a, b], v) = \frac{\left(\int_a^b P\{\Phi < \phi | \Lambda = \lambda, v\} f_\Lambda(\lambda) d\lambda \right)}{\int_a^b f_\Lambda(\lambda) d\lambda} \quad (27)$$

Figure 13 shows the cumulative distribution functions (CDFs) of DAFs with total probability and conditional probability at 400 km/h. The curve surges sharply at a low level of track irregularity, indicating that the DAF is less dispersed. At a high level of track irregularities, the curve increases slowly because of the high dispersion of DAFs.

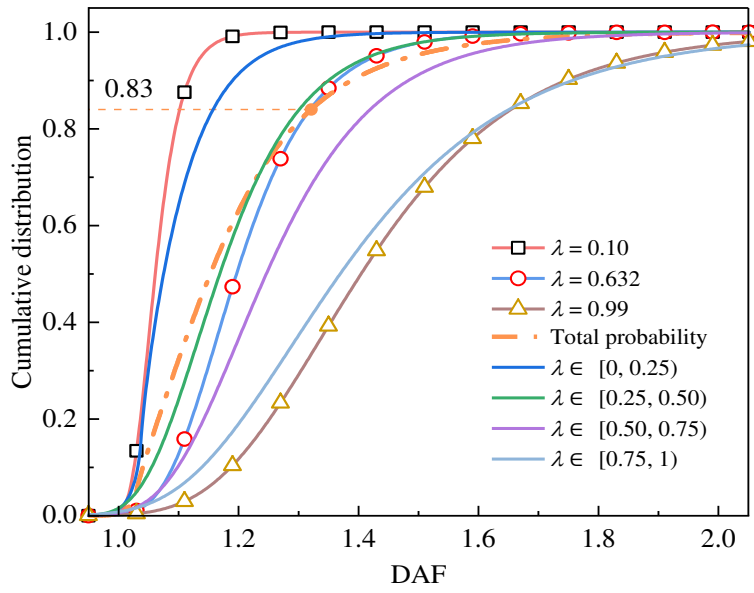


Figure 13. The cumulative distribution functions of dynamic amplification factors (DAFs)

Compared with the CDF at $\lambda = 0.632$, the CDF of total probability grows more slowly, and its DAF is smaller when the cumulative probability p is less than 0.83. The DAF is expected to be larger for extreme loads if the total probability is considered. For $\lambda \in [0.25, 0.50)$, $\lambda \in [0.25, 0.50)$, and $\lambda \in [0.75, 1)$, the DAFs with $p = 95\%$ are 1.42, 1.58, and 1.91 for 400 km/h, and the DAFs with $p = 75\%$ are 1.25, 1.36, and 1.55 for 400 km/h. The conditional probability distributions under different intervals of λ are significantly different and can better characterize the DAFs of different conditions.

5. Concluding remarks

A vertical vehicle–track coupled dynamics model was employed to examine the dynamic response of a railway slab-track foundation under moving train loads, with particular attention to the surface stress of the foundation. A three-parameter predictive model is used for determining the design values of DAFs to assist in track-foundation assessments. The future investigation would extend the proposed model to evaluate the variation of dynamic amplification factor along the depth. The following conclusions are drawn:

- a) The DAF of the surface stresses at different longitudinal positions obeys a Gumbel distribution with a right-skewed pattern. The Gumbel distribution better characterizes the random features

of the DAFs than the normal distribution.

- b) Normalized indices allow for the evolution of location and scale parameters with speed and track-spectrum cumulative probability to be captured. A three-parameter predictive model was developed for DAFs. For 400 km/h, the design DAFs predicted by the model are 2.16 and 1.36.
- c) The conditional probability distribution of DAFs for a particular line or interval can be determined by considering the spatial frequency coherence of track irregularities. This information is used to distinguish the standards of various rail lines. For lines whose $\lambda \in [0.25,0.50)$, $\lambda \in [0.25,0.50)$, and $\lambda \in [0.75,1)$, the DAFs are 1.42, 1.58, 1.91 under $p = 95\%$, and 1.25, 1.36, 1.55 under $p = 75\%$.

Acknowledgments

The study was supported by the National Natural Science Foundation of China (52078435), the Natural Science Foundation of Sichuan Province (2023NSFSC0391), the Royal Society (IEC\NSFC\211306 - International Exchanges 2021 Cost Share), the Key Laboratory of Mechanical Behavior Evolution and Control of Traffic Engineering Structures in Hebei (SZ2022-03), and the 111 Project (B21011).

References

- [1] Esveld C. Modern railway track. 2. ed. Zaltbommel: MRT-Productions; 2001.
- [2] Steenbergen MJMM, Metrikine AV, Esveld C. Assessment of design parameters of a slab track railway system from a dynamic viewpoint. J Sound Vib. 2007;306:361–371.
- [3] Ye Q, Luo Q, Feng G, Wang T, Xie H. Stress distribution in roadbeds of slab tracks with longitudinal discontinuities. Railw Eng Sci. 2022. doi:10.1007/s40534-022-00287-w
- [4] Zhou SH, Wang BL, Shan Y. Review of research on high-speed railway subgrade settlement in soft soil area. Railw Eng Sci. 2020, 28(2): 129-145.
- [5] Zhu SR, Wu LZ, Song XL. An improved matrix split-iteration method for analyzing underground water flow. Eng Comput. 2022. doi:10.1007/s00366-021-01551-z
- [6] Wang T, Luo Q, Liu J, et al. Method for slab track substructure design at a speed of 400 km/h. Transp Geotech. 2020;24:100391.

- [7] Feng G, Zhang L, Luo Q, Wang T, Xie H. Monitoring the dynamic response of track formation with retaining wall to heavy-haul train passage. *Int J Rail Transp.* 2022. doi:10.1080/23248378.2022.2103849
- [8] Luo Q, Wei M, Lu Q, Wang T. Simplified analytical solution for stress concentration ratio of piled embankments incorporating pile–soil interaction. *Railw Eng Sci.* 2021, 29(2): 199-210.
- [9] Nguyen VD, Luo Q, Wang T, et al. Monitoring of an instrumented geosynthetic-reinforced piled embankment with a triangular pile configuration. *Int J Rail Transp.* 2022. doi:10.1080/23248378.2022.2032853
- [10] Van Dyk BJ, Edwards JR, Dersch MS, et al. Evaluation of dynamic and impact wheel load factors and their application in design processes. *Proc Inst Mech Eng F J Rail Rapid Transit.* 2017;231:33–43.
- [11] Edwards JR, Cook A, Dersch MS, et al. Quantification of rail transit wheel loads and development of improved dynamic and impact loading factors for design. *Proc Inst Mech Eng F J Rail Rapid Transit.* 2018;232:2406–2417.
- [12] Japan Railway Technical Research Institute. Design standards for railway structures and other structures-concrete structures. 2004.
- [13] German Railway Standard Ril 836. *Erdbauwerke planen, bauen und instand halten* 2008.
- [14] Chen H, Luo Q, Zhang L, et al. Test analysis of vibration characteristics of high-speed railway on CRTS II slab ballastless track bridge-subgrade transition. *J Vib Shock.* 2014;33(1):81–88. [in Chinese]
- [15] Li J. Field test of subgrade-tunnel transition section of ballastless track on Suining-Chongqing railway and subgrade structure FEM calculation. Chengdu: Southwest Jiaotong University; 2008. [in Chinese]
- [16] Xiang YH. Field test on subgrade-culvert transition performance of ballastless track and subgrade FEM analysis on Suiyu railway. Chengdu: Southwest Jiaotong University; 2008. [in Chinese]
- [17] Yan SC. Test study on subgrade load performance and the road-culvert transition performance in Suiyu railway. Chengdu: Southwest Jiaotong University; 2007. [in Chinese]
- [18] Hu P, Zhang C, Chen SJ, et al. Dynamic responses of bridge–embankment transitions in high

speed railway: Field tests and data analyses. *Eng Struct.* 2018;175:565–576.

- [19] Ye YS, Cai DG, Wei SW, et al. Distribution characteristics and analytical method of dynamic stress on subgrade of ballastless track for high-speed railway. *China Railway Sci.* 2020;41(6):1–9. [in Chinese]
- [20] Bian X, Jiang H, Cheng C, et al. Full-scale model testing on a ballastless high-speed railway under simulated train moving loads. *Soil Dyn Earthq Eng.* 2014;66:368–384.
- [21] Woodward PK, Laghrouche O, Mezher SB, et al. Application of coupled train-track modelling of critical speeds for high-speed trains using three-dimensional non-linear finite elements. *Int J Railw Technol.* 2015;4:1–35.
- [22] Chen M, Sun Y, Zhu S, et al. Dynamic performance comparison of different types of ballastless tracks using vehicle-track-subgrade coupled dynamics model. *Eng Struct.* 2021;249:113390.
- [23] Dong K, Connolly DP, Laghrouche O, et al. The stiffening of soft soils on railway lines. *Transp Geotech.* 2018;17:178–191.
- [24] Connolly DP, Dong K, Alves Costa P, et al. High speed railway ground dynamics: a multi-model analysis. *Int J Rail Transp.* 2020;8:324–346.
- [25] Dong K, Connolly DP, Laghrouche O, et al. Non-linear soil behaviour on high speed rail lines. *Comput Geotech.* 2019;112:302–318.
- [26] Berggren EG, Li MXD, Spännar J. A new approach to the analysis and presentation of vertical track geometry quality and rail roughness. *Wear.* 2008;265:1488–1496.
- [27] Charoenwong C, Connolly DP, Woodward PK, et al. Analytical forecasting of long-term railway track settlement. *Comput Geotech.* 2022;143:104601.
- [28] Charoenwong C, Connolly DP, Odolinski K, et al. The effect of rolling stock characteristics on differential railway track settlement: an engineering-economic model. *Transp Geotech.* 2022;37:100845.
- [29] Zhai W. *Vehicle–track coupled dynamics: theory and applications.* Singapore: Springer; 2020.
- [30] Zhai W, Wang K, Cai C. *Fundamentals of vehicle–track coupled dynamics.* *Veh Syst Dyn.* 2009;47:1349–1376.
- [31] Zhai W, Xia H, Cai C, et al. High-speed train–track–bridge dynamic interactions – Part I:

- theoretical model and numerical simulation. *Int J Rail Transp.* 2013;1:3–24.
- [32] Zhai W, Han Z, Chen Z, et al. Train–track–bridge dynamic interaction: a state-of-the-art review. *Veh Syst Dyn.* 2019;57:984–1027.
- [33] Chen G, Zhai WM. A new wheel/rail spatially dynamic coupling model and its verification. *Veh Syst Dyn.* 2004;41:301–322.
- [34] Xu L, Zhai W. A novel model for determining the amplitude-wavelength limits of track irregularities accompanied by a reliability assessment in railway vehicle-track dynamics. *Mech Syst Sig Process.* 2017;86:260–277.
- [35] Yang J, Zhu S, Zhai W. A novel dynamics model for railway ballastless track with medium-thick slabs. *Appl Math Modell.* 2020;78:907–931.
- [36] Xu L, Zhai W. Train–track coupled dynamics analysis: system spatial variation on geometry, physics and mechanics. *Railw Eng Sci.* 2020;28:36–53.
- [37] Xu L, Zhai W, Gao J. A probabilistic model for track random irregularities in vehicle/track coupled dynamics. *Appl Math Modell.* 2017;51:145–158.
- [38] National Railway Administration of the People's Republic of China. PSD of ballastless track irregularities or high-speed railway. 2014. [in Chinese]
- [39] Chen G, Zhai WM, Numerical simulation of the stochastic process of railway track irregularities, *J. Southwest Jiaotong Univ.* 1999; 34(2), pp. 138–142. [in Chinese]
- [40] Fan SB. Analysis on experiment of dynamic response in ballastless track subgrade of high speed railway. Chengdu: Southwest Jiaotong University; 2010. [in Chinese]
- [41] Lamprea-Pineda AC, Connolly DP, Hussein MFM. Beams on elastic foundations – A review of railway applications and solutions. *Transp Geotech.* 2022;33:100696.
- [42] Alfredo H-SA, Wilson H. Probability concepts in engineering planning and design. Canada: Wiley; 1975.
- [43] Mei H, Leng W, Nie R, et al. Random distribution characteristics of peak dynamic stress on the subgrade surface of heavy-haul railways considering track irregularities. *Soil Dyn Earthq Eng.* 2014;66:368–384.
- [44] Wang P, Wang Y, Tang H, et al. Error theory of chord-based measurement system regarding track

- geometry and improvement by high frequency sampling. *Measurement*. 2018;115:204–216.
- [45] Wang Y, Tang H, Wang P, et al. Multipoint chord reference system for track irregularity: Part I – Theory and methodology. *Measurement*. 2019;138:240–255.
- [46] Connolly DP, Kouroussis G, Laghrouche O, Ho CL, Forde MC. Benchmarking railway vibrations - Track, vehicle, ground and building effects. *Constr Build Mater*. 2015, 92: 64-81.
- [47] Hu J, Bian X, Xu W, Thompson D. Investigation into the critical speed of ballastless track. *Transp Geotech*. 2019; 18: 142-148.
- [48] Ling L, Jiang P, Wang K, Zhai W. Nonlinear stability of rail vehicles traveling on vibration-attenuating slab tracks. *J Comput Nonlin Dyn*. 2020; 15(7): 071005.